To be submitted to JGR-Atmosphere 05/22/2023

Observations of Typhoon Generated Gravity Waves from the CIPS and AIRS instruments and comparison to the high-resolution ECMWF model.

Chihoko Y. Cullens[1], Brentha Thurairajah[2], Scott L. England[3],
Cora E. Randall[1], Jia Yue[4], Corwin Wright[5]

1. University of Colorado at Boulder, Laboratory for Atmospheric and Space Physics
2. Bradley Department of Electrical and Computer Engineering, Center for Space Science and Engineering Research, Virginia Tech, Blacksburg, Virginia
3. Aerospace and Ocean Engineering, Virginia Tech, Blacksburg, Virginia
4. NASA Goddard Space Flight Center
5. Centre for Space, Atmospheric and Oceanic Science, University of Bath, Bath, UK

Key Points

(1) CIPS and AIRS measurements of concentric GWs generated by Typhoon Yutu are used to verify ECMWF GWs in the altitude range of 30-55 km.

(2) Analysis of GW observations from CIPS and AIRS as well as ECMWF data provides detailed characteristics of concentric GWs.

(3) Differences in GW amplitudes among five typhoon cases grow as GWs propagate upward, indicating the importance of background winds.

Abstract

The satellite-based Cloud Imaging and Particle Size (CIPS) instrument and Atmospheric Infrared Sounder (AIRS) observed concentric gravity waves (GWs) generated by Typhoon Yutu in late October, 2018. This work compares CIPS and AIRS nadir viewing observations of GWs at altitudes of 50-55 km and 30-40 km, respectively, to simulations from the high-resolution European Centre for Medium-Range Weather Forecasting Integrated Forecasting System (ECMWF-IFS) and ECMWF reanalysis v5 (ERA5). Both ECMWF-IFS with 9 km and ERA5 with 31 km horizontal resolution show concentric GWs at similar locations and timing as the AIRS and CIPS observations. The GW wavelengths are ~225-236 km in ECMWF-IFS simulations, which compares well with the wavelength inferred from the observations. After validation of ECMWF GWs, five category 5 typhoon events during 2018 are analyzed using ECMWF to obtain characteristics of concentric GWs in the Western Pacific regions. The amplitudes of GWs in the stratosphere are not strongly correlated with the strength of typhoons, but are controlled by background wind conditions. Our results confirm that amplitudes and shapes of concentric GWs observed in the stratosphere and lowermost mesosphere are heavily influenced by the background wind conditions.

Plain Language Summary

Atmospheric gravity waves (GWs) have an important role in coupling the different atmospheric layers. One of the main sources of GWs is convection such as typhoons. In the stratosphere, these GWs frequently appear as concentric (or ring-shaped) patterns in nadir-viewing satellite measurements. In this work, data from two such nadir viewing satellite instruments, the

Cloud Imaging and Particle Size (CIPS) instrument and Atmospheric Infrared Sounder (AIRS), are analyzed to study the GWs generated by typhoon Yutu, which occurred in late October 2018. CIPS and AIRS observe at altitudes of 50-55 km and 30-40 km, respectively, providing us a unique opportunity to study concentric GWs at two different altitudes. The satellite observations are then used to validate the GW-resolving high-resolution European Centre for Medium-Range Weather Forecasting (ECMWF) model. Utilizing ECMWF simulations, 4 more typhoon events were analyzed. The results indicate that the amplitudes of concentric GWs in the stratosphere are not correlated with the strength of typhoons. However, the amplitudes and shapes of concentric GWs observed in the stratosphere and lower mesosphere are found to be influenced by the background wind conditions. This work provides an understanding of the relative importance of GW source strength and background wind conditions.

1. Introduction

Gravity waves (GWs) transport momentum and energy from the lower atmosphere to the upper atmosphere and drive atmospheric circulations [e.g., Fritts & Alexander, 2003; Alexander et al., 2010]. The main sources of GWs are frontal systems, convection, orography, and spontaneous emission from unstable jets. Convectively generated GWs have been studied using various satellite and ground-based observations and high-resolution models [e.g., Alexander & Pfister, 1995; Kim & Chun, 2011; Yue et al., 2009]. Strong convective activity, including hurricanes and typhoons, generates GWs that appear as concentric (or ring-shaped) patterns in nadir-viewing satellite measurements, ground-based imager observations and high-resolution simulations [e.g., Yue et al., 2009, 2013; Kim et al., 2009; Liu et al., 2014; Gong et al., 2015]. Convectively generated GWs can propagate up to the mesosphere and lower thermosphere (MLT), and even higher into the thermosphere and ionosphere, and cause large disturbances in winds and electron densities in the upper atmosphere [e.g., Vadas & Liu, 2013; Liu & Vadas, 2013; Azeem et al., 2015]. Furthermore, typhoon-generated GWs can feed back to the development of the typhoon itself [e.g., Kim & Chun, 2011; Hoffmann et al., 2018]; by affecting wind structure, typhoon-generated GWs can intensify the typhoon during the development stage of the typhoon [Kim & Chun, 2011]. Therefore, it is important to characterize these convectively generated GWs in order to understand their impacts on the lower and also upper atmosphere.

The nadir-viewing Cloud Imaging and Particle Size (CIPS) instrument on the Aeronomy of Ice in the Mesosphere (AIM) satellite measures perturbations in Rayleigh scattered ultraviolet radiation that are indicative of GW-induced variations at altitudes of ~50-55 km [Randall et al., 2017; Forbes et al., 2021; 2022]. These Rayleigh Albedo Anomaly (RAA) data show clear concentric GWs in late October 2018, coincident with the occurrence of Typhoon Yutu. The nadir-viewing Atmospheric Infrared Sounder (AIRS) instrument measures perturbations in brightness temperature that are indicative of GW-induced variations at altitudes of ~30-40 km. [e.g., Hoffmann et al., 2013; Gong et al., 2015]. AIRS data also revealed concentric GWs in late October 2018. By combining analyses of data from both CIPS and AIRS, we can probe altitude variations of concentric GWs in the middle stratosphere and lowermost mesosphere.

In this work, we combine CIPS and AIRS observations to study GWs generated by typhoon Yutu. The high-resolution European Centre for Medium-Range Weather Forecasts Integrated Forecasting System (ECMWF-IFS) dataset is also used to supplement the observational study. Gong et al. [2015] conducted a study of concentric GWs with both AIRS and ECWMF, using automated detections of concentric GWs globally to investigate hemispheric differences of concentric GWs in July and January. Their study showed that concentric GW phases and wavelengths from ECMWF simulations and AIRS observations are comparable; however, amplitudes of ECMWF GWs are weaker than those from AIRS observations. Since the work by Gong et al. [2015], the ECMWF horizontal resolution has been improved from 16 km to 9 km, and the number of vertical levels has been increased from 91 levels to 137 levels, with the same top pressure level at 0.01 hPa. The hourly ECMWF Reanalysis v5 (ERA5) has ~31-km horizontal resolution and also has been used for GW studies [e.g., Cullens & Thurairajah, 2021]. This work evaluates GWs resolved by the updated version of ECMWF-IFS and ERA5 simulations via comparisons against CIPS and AIRS observations. We also focus on individual strong typhoon events in ECMWF, and obtain characteristics of typhoon-generated GWs including wavelengths, altitude variations and time evolution of GWs.

In this paper, explanations of data sets are summarized in Section 2. Section 3 provides results of GWs generated by Typhoon Yutu in October 2018 from both satellite observations and ECMWF simulations. GW characteristics from five different typhoon events are summarized in Section 4. Conclusions are presented in Section 5.

2. Data

2.1. ECMWF

ECMWF provides global analysis of atmospheric data from the ground to the lower mesosphere. The cycle 41r2 version of the ECMWF-IFS high-resolution model is used here and referred as ECMWF. ECMWF has ~9 km horizontal resolution with 137 vertical levels from the ground to 0.01 hPa. This version of ECMWF is capable of resolving mesoscale GWs with horizontal scales larger than ~70 km [Preusse et al., 2014]. Although ECMWF extends up to ~80 km, amplitudes of GWs are suppressed above ~45 km due to a sponge layer [Schroeder et al., 2009, Ehard et al., 2017; Gisinger et al., 2022]. Earlier versions of ECMWF GWs have been validated against AIRS, SABER, and COSMIC satellite observations, lidar and radiosonde ground-based observations, and other high-resolution models including the Weather Research and Forecasting (WRF) model [e.g., Alexander & Teitelbaum, 2007; Schroeder et al., 2009; Kim et al., 2009; Wu & Eckermann, 2008; Yamashita et al., 2010]. The 6-hourly ECMWF is used in this study. The hourly ECMWF Reanalysis v5 (ERA5) dataset provided by ECMWF, with ~31 km horizontal resolution, is also used in this work for comparison [Hersbach et al., 2020]. Temporal variations of GWs from ERA5 have been validated previously against COSMIC GW data [e.g., Cullens et al., 2021].

Both ERA5 and ECMWF GW perturbations are estimated by removing large-scale variations from the zonal wind (u) and vertical wind (w). Large-scale variations are estimated by averaging over 15° longitude x 15° latitudes regions at each grid and each pressure level for both ERA5 and ECMWF. Approximate altitudes are estimated using geopotential height. It should be noted here that AIRS data is used in assimilation process for ECMWF data product. Yamashita et al. [2010] compared ECMWF GW amplitudes between analysis and various forecast time to examine assimilation influences on resolved GWs in ECMWF. Although Yamashita et al. [2010] presented no clear sign of increase in GW amplitudes by assimilated process for climatology of GWs, further analysis of assimilation influences on GW need to be conducted in the future.

2.2. AIM-CIPS

The CIPS instrument is onboard the AIM satellite, which was launched in April 2007 [Rusch et al., 2009; Russell et al., 2009]. CIPS observes Polar Mesospheric Clouds (PMCs) in the summer by subtracting the background Rayleigh scattering from the ice particle scattering by

PMCs (if present) [Bailey et al., 2009; Lumpe et al., 2013]. In the absence of PMCs, perturbations to the observed Rayleigh scattering signal, reported as RAA, are indicative of GW-induced variations at 50-55 km altitude. The data are measured by four cameras with a total cross-track by along-track field of view of 80° × 120° (~1000 km × 2000 km), and a resolution of 7.5 km x 7.5 km. The CIPS-RAA measurement spans ~40°–85° latitude in the spring and summer hemisphere during 2007-2015. Due to a change in operating mode in February 2016, the CIPS observations after this change are global in sunlit regions year-round, except where PMCs are present [Randall et al., 2017].

To quantify GW-induced perturbations to the Rayleigh scattering signal (controlled by atmospheric neutral density and ozone), the RAA is calculated as the difference between the observed Rayleigh scattering albedo and a baseline albedo that would be observed in the absence of any small-scale atmospheric variations. More information on the retrieval process can be found in Randall et al. [2017]. The RAA retrievals are sensitive to GW perturbations with horizontal wavelengths of ~15–600 km and with vertical wavelengths ≥15 km. CIPS RAA data used in this work are available from the CIPS website (http://lasp.colorado.edu/aim/) [Randall et al., 2017].

2.3. AIRS

AIRS is a nadir-sounding infrared radiometer on NASA's Aqua satellite. Data is available from 2002 onwards [Aumann et al., 2003]. Stratospheric GWs are derived from emitted radiance measurements in the 4.3 μm CO_2 fundamental band, which is most sensitive to 30-40 km altitude. GW perturbations are extracted by removing background temperature and large-scale planetary waves [Hoffmann et al., 2013] using a fourth-order cross-track polynomial. A detailed GW analysis method can be found in Hoffmann et al. [2013], and all processed GWs can be found at https://data.fz-juelich.de/dataset.xhtml?persistentId=doi:10.26165/JUELICH-DATA/LQAAJA. AIRS observations are sensitive to GWs with vertical wavelengths longer than 10-15 km and horizontal wavelength longer than 30-80 km.

3. Results of Typhoon Yutu Generated Gravity Waves

Typhoon Yutu occurred from October 22-31, 2018 in the western Pacific Ocean (10°N-20°N latitudes and 115°E-155°E longitudes). The path of Typhoon Yutu is shown in Figure 1a and the 10-minute averaged maximum sustained wind speed is shown in Figure 1b. Maximum sustained wind speed is the maximum value of the average wind speed at the surface and is often used to characterize typhoon activity according to the World Meteorological Organization (WMO). Typhoon locations and 10-minute averaged maximum sustained wind speed data are obtained from the Japan Meteorological Agency (JMA) (http://www.jma.go.jp/jma/jma-eng/jma-center/rsmc-hp-pub-eg/besttrack.html). Typhoon Yutu traveled westward and reached maximum wind speed on October 24. JMA categorized Typhoon Yutu as a “violent typhoon”, defined as having a maximum sustained wind speed over 105 kt (54 m/s); specifically, the maximum wind speed for Typhoon Yutu was 115 kt, which meets the WMO specification of a “Super Typhoon”. Such typhoons are also referred to as “Category 5 Super Typhoons”.

Figure 2 shows GW observations from CIPS (50-55 km altitude) and AIRS (30-40 km) as well as GWs in the simulated vertical wind perturbation at ~50 km and ~30 km altitude from ERA5 (31 km horizontal resolution) and high-resolution ECMWF (9 km horizontal resolution). AIRS observations were made on October 27, 2018 at 13:30 LT (~4:30 UT) and CIPS observations were made on October 26, 2018 around 22:25 UT. ECMWF and ERA5 simulations pertain to October 27, 2018 at 00 UT; the ECMWF archive their analyses only every 6 hours, so 00 UT is the closest time to the CIPS and AIRS observations. Although ERA5 has an hourly data, to be consistent with ECMWF data, ERA5 was used at the same time as ECMWF data in Figure 2. Both AIRS and CIPS observations capture clear concentric GW structures associated with Typhoon Yutu. The ERA5 and ECMWF simulations both show similar concentric GWs at the same location as the AIRS and CIPS observations. As expected, the higher-resolution ECMWF simulation in Figures 2c and 2d shows finer-scale GW structures than the lower resolution ERA5 simulation in Figures 2e and 2f. To compare ERA5 and ECMWF GW amplitudes, GW amplitudes are averaged within the red boxes indicated in Figures 2c-f. ECMWF and ERA5 GW amplitude at 10 hPa (~30 km) are 3.2 cm/s and 2.0 cm/s, respectively. Averaged ERA5 GW amplitude is 38% smaller than averaged ECMWF GW amplitude at 10 hPa. At 1 hPa, averaged GW amplitudes are 8.2 cm/s and 4.7 cm/s for ECMWF and ERA5, respectively. ERA5 GW amplitudes are 41% smaller than ECMWF GWs.

Liu et al. [2014] showed clear convectively generated concentric GWs using a high-resolution version of the Whole Atmosphere Community Climate Model (WACCM) with ~25 km horizontal resolution, indicating that model resolutions of ~25 km can resolve somewhat reasonable concentric GWs generated by typhoons. Gong et al. [2015] compared concentric GW structures and amplitudes simulated with ECMWF using both 25 km and 16 km horizontal resolution. Their results indicate that the structure of the concentric GWs is similar in the two resolution datasets, but the GW amplitudes are larger, and closer to those observed, in the 16 km resolution dataset. Our results are consistent with Gong et al. [2015], so the rest of this work was conducted mainly using the 9 km horizontal resolution ECMWF output.

Figure 2 shows that the concentric GWs observed by CIPS at 50-55 km extend farther horizontally than those observed by AIRS at 30-40 km, and this appears to be evident in the

ECMWF results as well. To confirm the latter, ECMWF simulations in ~10-km increments from 20 to 60 km are shown in Figure 3. Figures 3b and 3d are repeated from Figures 2d and 2c, respectively. As expected, the horizontal extent of concentric GWs expands as the waves propagate upward, consistent with the CIPS and AIRS observations shown in Figures 2a-b. Amplitudes of concentric waves are getting weaker above 0.8 hPa level (~55 km) and wave structures are significantly weakened and disappeared above 0.25 hPa level (~60 km), which we believe is due to damping in ECMWF at higher altitudes by the sponge layers discussed by previous studies [e.g., Ehard et al., 2017; Gisinger et al., 2022]. Gisinger et al. [2022] observed that above ~45 km the amplitudes of GWs in ECMWF are weaker than in lidar observations. Although GW amplitudes might be reduced above ~45 km, our results indicate that GW structures are reasonably simulated compared to CIPS around 50-55 km.

To further compare AIRS, CIPS, and ECMWF GWs, spectrum analysis of horizontal scale is shown in Figure 4. Horizontal wavelength (λ_h) along red lines in Figures 4a, 4c, 4e are ~237 km, 247 km, 236 km for AIRS at 35-40 km altitudes, CIPS at 50-55 km altitudes, and ECMWF at ~50 km, respectively. It is not shown but ECMWF λ_h at ~30 km altitudes is 225 km. Horizontal wavelengths are consistent between AIRS, CIPS and ECMWF. Averaged λ_h is 240 km.

One of the advantages of combining both observations and simulations is to supplement information that these observations cannot obtain, such as the vertical wavelength, time-evolution, and altitudinal variations of GWs. Figure 5 shows the time-evolution of GW signatures in the ECMWF vertical wind at 3 hPa (~40 km) and at 300 hPa (~15 km) from October 23 to October 31 at 12 UT. From October 25 (Figure 5b) to October 29 (Figure 5d), concentric GW structures move westward and almost disappear on October 31 (Figure 5e). At lower altitudes at 10 km, GW structures are not as spread-out as GWs at 40 km and also disappear by October 31 (Figure 5k). At 40 km, GW amplitudes maximize around October 27 (Figure 5c).

Figure 6a shows a concentric GW signature in the vertical wind at an altitude of ~35 km from the ECMWF simulation. A vertical slice in Figure 6b is made along the white transect in Figure 6a. Clear GW structures are seen from the lower altitudes up to ~60 km. The vertical wavelength estimated from Figure 6b is ~10-14 km, depending on location. GW structures at the higher altitudes are more spread out than those at lower altitudes, which is consistent with the difference in GW structures from CIPS at 50-55 km and AIRS at 30-40 km shown in Figure 2.

To better understand changes in GW amplitudes and GW responses to the evolution of a typhoon event, Figure 7 shows temporal variations of the averaged of GW amplitudes in the ECMWF and ERA5 vertical wind (Figure 7a and 7b, respectively), along with the maximum sustained wind speed during Typhoon Yutu (Figure 7c). GW amplitudes are averaged within +/- 15° longitude and latitude range from the center of a typhoon event at each time step to focus on typhoon generated GWs. ERA5 provides hourly data in contrast to 6-hourly ECMWF data, resulting in more data points in the ERA5 results in Figure 7b. Both ECMWF and ERA5 GW amplitudes show the largest peak on October 27-28, which is a few days after the peak wind speed on October 24-25. GW amplitudes significantly decay after October 30 as the typhoon weakened. There are several smaller peaks on October 25 and October 29 in Figure 7a, and they are coincident with peaks in wind speeds. To explain the temporal delay in GW amplitudes and typhoon activity, vertical group velocity is calculated using the following equation,

$$w_g = -\frac{Nmk}{(k^2+m^2)^{\frac{3}{2}}} \qquad (1)$$

where N is The Brunt–Väisälä frequency, m is vertical wavenumber, and k is horizontal wavenumber [e.g., Yue et al., 2009]. Based on typhoon Yutu characteristics (wavelengths) from

Figure 6, estimated w_g is 0.9-1.2 m/s, and it takes ~10-12 hours to get to 40 km. Based on this calculations, vertical velocity itself cannot explain the 1-2 days of delay in the peak of gravity wave amplitudes compared to maximum wind speeds. However, small two peaks in GW vertical wind amplitudes on October 25 and 29 can be explained by the strength of typhoon. Background wind conditions that are suitable for wave propagation most likely contributed to the enhancements on October 27.

Temporal variations of GW vertical wind amplitude from ERA5 and ECMWF show very similar variations. However, ECMWF shows a peak on October 29 not seen in ERA5 GWs. ERA5 GW amplitudes are generally smaller than ECMWF GW amplitudes. Averaged GW amplitudes from October 22 to November 1 at 40 km (30 km) altitudes shown in Figure 7 are 4.4 cm/s (2.6 cm/s) and 2.7 cm/s (1.7 cm/s) for ECMWF and ERA5, respectively. ERA5 amplitudes are 39% and 35% smaller than ECMWF GWs at 40 km and 30 km altitudes, respectively, due to coarse resolutions of ERA5.

Altitude variations of momentum fluxes are shown in Figure 8 at 2 hPa (~45 km), 5 hPa (~35 km), 10 hPa (~30 km), and 50 hPa (~17 km). Momentum Flux (MF) is calculated using the following equation.

$$MF = \rho_0 \overline{u' \ w'} \qquad (2)$$

where ρ_0 is atmospheric density, u' is zonal wind perturbation, and w' is vertical wind perturbation. At higher altitudes (Figures 8a-b), the westward (negative) momentum flux is clear on the western side of the concentric GW, whereas at lower altitudes (Figures 8c-d), both the eastern and western sides reveal strong momentum fluxes with similar magnitude, but opposite direction. This anti-symmetric GW pattern that develops at higher altitudes is caused by background wind conditions that affect GW propagation between 17 km and 30 km [e.g., Piani et al.,2000; Yue et al., 2009;

Kim et al., 2009; Vadas et al., 2009]. There are strong south-eastward winds at 35 and 40 km in Figure 8a and 8b. Under eastward wind conditions, it is easier for westward propagating GWs to propagate upward because phases tilts vertically and vertical wavelengths get longer [Fritts & Alexander, 2003]. Such background wind conditions can cause an asymmetric GW pattern at higher altitudes.

4. Five Typhoon Cases in 2018.

Based on the validation of ECMWF GWs for Typhoon Yutu against CIPS and AIRS, we further expanded our analysis to four additional typhoon events that occurred in 2018, specifically Typhoon Jebi (August 26-September 4), Typhoon Mangkhut (September 6 – September 17), Typhoon Kong-Rey (September 28 – October 6), and Typhoon Trami (September 20 to October 1). These typhoon events are all categorized as the strongest typhoon category, i.e. ("Violent typhoon") by JMA and "Category 5 typhoon" by NOAA. Table 1 summarizes the characteristics of these typhoon events, including maximum wind speeds and duration of wind speeds over 100 kt to better understand typhoon activity.

Figure 9 shows snapshots of GW structures in the ECMWF vertical wind at an altitude of ~35 km (5 hPa), vertical slices of the GW structures, and their power spectrum for each typhoon event. Figure 9 shows results of Typhoon Jebi on September 2, 2018, Typhoon Mangkhut on September 14, 2018, Typhoon Kong-Rey on October 2, 2018 and Typhoon Trami on September 28, 2018. These dates are selected based on the largest GW activity when typhoons are evident at 5 hPa, and dates are indicated in Table 1 as "GW analysis date". Based on Figure 9, GW characteristics from all cases are obtained and summarized in Table 1. The average horizontal wavelength from the five typhoon-generated GWs is 236 km, with a range from 150 km to 400 km. GW vertical wavelengths range from 10 km to 17 km. Wu et al. [2015] derived a vertical wavelength of 6-12 km from WRF simulations of Typhoon Mindulle in 2004, which is similar to our study.

All four additional typhoon cases show concentric GWs at ~35 km altitude, though only part of the concentric GWs propagate up to 35 km and appear in Figure 9. For example, concentric GWs generated by Typhoon Kong-Rey (Figure 9c) show larger amplitudes in the southeast GW region, but GWs generated by Typhoon Trami (Figure 9d) show larger amplitudes in the east GWs. Figure 10 shows horizontal wind magnitudes and amplitudes along with vertical wind perturbation at 35 km. Out of the 5 cases, typhoon Yutu is the only case where westward propagating waves remained at 35 km, while the other four cases show that eastward propagating waves remained at 35 km. In Figure 10a for Typhoon Yutu case, it is clear that strong eastward winds exist, and that the GWs are propagating against it. Typhoon Jebi (Figure 10b), Mangkhut (Figure 10c) and Typhoon Trami (Figure 10e) all show relatively large westward winds, and GWs are propagating against such winds as indicated by red arrows. For Typhoon Kong-Rey case, there are north-westward winds and GWs are propagating south-east, opposite to the wind directions. When GWs propagates against wind directions, all intrinsic phase speed, vertical wavelength and intrinsic frequency become larger [Fritts & Alexander, 2003]. Large intrinsic frequency or shorter period causes more vertical propagation, and GWs with longer vertical wavelength are less subject to dissipation [Fritts & Alexander, 2003]. AIRS and CIPS observe more GWs with longer vertical wavelength due to observational filtering. Such waves are therefore easier to be observed by AIRS and CIPS nadir viewing instruments.

In addition to GW wavelengths, vertical wind amplitudes of GWs are also calculated and summarized in Table 1. GW amplitudes at 3 hPa (~20 km) and 50 hPa (~40 km) in Table 1 are calculated by the following steps. First, vertical wind GW perturbations are averaged within +/- 15° latitude and longitude from the center of the typhoon indicated by JMA's typhoon location data at each time step. Then the largest GW amplitudes at 20 km and 40 km in Table 1 are selected within 3 days of GW analysis date. Various grid sizes have been tested. Although absolute values of GW amplitudes vary, conclusions from this analysis remain consistent. From Table 1, maximum wind speeds are largest during typhoons Yutu and Kong-Rey; however, GWs during Typhoon Mangkhut have the largest amplitudes at 20 km. Also, GW amplitudes for the three typhoons with the shortest duration of winds > 100 kt vary from smallest to second largest. By comparing GW amplitudes at 20 km and 40 km, the largest GW amplitudes changed from GWs generated by Typhoon Mangkhut at 20 km to GWs generated by Typhoon Jebi at 40 km. For these five cases, the strength of GWs in the stratosphere do not seem to correlate with the characteristics of typhoons.

Furthermore, at 20 km the maximum GW amplitude is 2.8 cm/s during Typhoon Mangkhut, and the minimum GW amplitude is 2.2 cm/s during Typhoon Yutu. The difference between the maximum and minimum amplitude is 21%. At 40 km, the maximum and minimum GW amplitudes are 8.1 and 4.4 cm/s during typhoons Jebi and Kong-Rey, respectively. The difference here is 46%. The GW amplitude differences grow as the GWs propagate upward. These results indicate that differences in GW amplitudes between different typhoon cases at ~40 km are influenced by background winds that affect GW propagation between 20 km and 40 km. Therefore, whether typhoon generated GWs may impact the upper atmosphere is highly dependent on the seasonality of the typhoons and background winds through which the waves subsequently propagate.

5. Summary & Conclusion

This work combines CIPS and AIRS nadir viewing observations at 50-55 km and 30-40 km, respectively, and the high-resolution ECMWF model data to study the altitudes and temporal evolution of concentric GWs. Both AIRS and CIPS captured clear concentric GW structures during Typhoon Yutu in late October 2018, with horizontal wavelength of ~237-247 km. ECMWF-IFS (a horizontal resolution of 9 km) and ERA5 (a horizontal resolution of 31 km) are able to generate concentric GWs at similar locations and timing as the AIRS and CIPS observations. The GW horizontal wavelength simulated by the ECWMF-IFS was also ~225-236 km. Further analysis of ECMWF data showed that the vertical wavelength of these concentric GWs was ~10 – 14 km, and GW amplitudes reached a maximum ~1-2 days after the peak wind speed of typhoon Yutu.

After a validation case study of ECWMF GWs against CIPS and AIRS observations, four additional category 5 typhoons were analyzed to obtain characteristics of concentric GWs generated by these typhoons. ECMWF captured clear concentric GW structures generated by all five cases. Analysis of all five cases showed an averaged horizontal wavelength of 237 km, ranging from 150 km to 400 km, and vertical wavelength ranging from 10 km to 17 km. Differences in maximum and minimum GW amplitudes among the five typhoon cases grow as GWs propagate upward.

Our analysis also shows that the amplitudes of GWs in the stratosphere are not strongly correlated with the strength of typhoons as indicated by wind. Our results confirm that typhoon-generated concentric GWs in the stratosphere and lowermost mesosphere where AIRS and CIPS observe have more influences from background wind conditions than strength of typhoons for our cases. This work has shown that combining analyses of CIPS and AIRS data enables verification of model simulations of GW propagation across the stratopause, a prerequisite to understanding how GWs act to couple the lower and upper atmosphere and ionosphere.

Acknowledgement

We thank Dr. Justin Carstens for the CIPS GW retrievals. AIM is funded by the NASA Small Explorer program. AIRS GW data are produced by Dr. Lars Hoffmann. CYC was supported by NSF AGS award #2217461 and NASA Heliophysics Supporting Research (80NSSC22K0895) and NASA ECIP (80NSSC22K0726). CER was supported by AIM, the NASA DRIVE program (80NSSC20K0628) and the NASA Heliophysics Guest Investigator program (80NSSC18K0775). BT was supported by NASA/AIM. CJW is supported by Royal Society University Research Fellowship URF\R\221023 and NERC grant NE/S00985X/1.

Open Research

Data Availability Statement

CIPS RAA used in this work is available from the CIPS website (http://lasp.colorado.edu/aim/) [Randall et al., 2017]. AIRS GW data are produced by Dr. Lars Hoffmann, and obtained from https://data.fz-juelich.de/dataset.xhtml?persistentId=doi:10.26165/JUELICH-DATA/LQAAJA [Hoffmann, 2021]. Locations and maximum sustained wind speed data are obtained from Japan Meteorological Agency (http://www.jma.go.jp/jma/jma-eng/jma-center/rsmc-hp-pub-eg/besttrack.html) [Japan Meteorological Agency, 2018]. ECMWF and ERA5 were provided by ECMWF Meteorological Archival and Retrieval System (MARS) at https://www.ecmwf.int/en/forecasts/datasets [European Centre for Medium-Range Weather Forecasts, 2016, 2019].

References

Alexander, M. J., M. Geller, C. McLandress, S. Polavarapu, P. Preusse, F. Sassi, K. Sato, S. Eckermann, M. Ern, A. Hertzog, Y. Kawatani, M. Pulido, T. Shaw, M. Sigmond, R. Vincent, S. Watanabe (2010), Recent developments in gravity wave effects in climate models, and the global distribution of gravity wave momentum flux from observations and models, *Q. J. Roy. Meteorol. Soc.,* 136, 1103-1124.

Alexander, M. J., and L. Pfister (1995), Gravity wave momentum flux in the lower stratosphere over convection, Geophys. Res. Lett., 22, doi:10.1029/95GL01984.

Alexander, M. J., and H. Teitelbaum (2007), Observation and analysis of a large amplitude mountain wave event over the Antarctic peninsula, *J. Geophys. Res*., 112, D21103, doi:10.1029/2006JD008368.

Aumann, H. H., et al. (2003), AIRS/AMSU/HSB on the Aqua Mission: Design, science objectives, data products and processing systems, IEEE Trans. Geosci. Remote Sens., 41, 253– 264.

Azeem, I., J. Yue, L. Hoffmann, S. D. Miller, W. C. Straka III, and G. Crowley (2015), Multisensor profiling of a concentric gravity wave event propagating from the troposphere to the ionosphere, *Geophys. Res. Lett*., 42, 7874–7880, doi:10.1002/ 2015GL065903.

Bailey, S. M., G. E. Thomas, D. W. Rusch, A. W. Merkel, C. D. Jeppesen, J. N. Carstens, C. E. Randall, W. W. McClintock, and J. M. Russell III (2009), Phase functions of polar mesospheric cloud ice as observed by the CIPS instrument on the AIM satellite, J. Atmos. Sol. Terr. Phys., 71, 373–380, doi:10.1016/j.jastp.2008.09.039.

Cullens, C. Y., & Thurairajah, B. (2021). Gravity wave variations and contributions to stratospheric sudden warming using long-term ERA5 model output. Journal of Atmospheric and Solar-Terrestrial Physics, 219, 105632. https://doi.org/10.1016/j.jastp.2021.105632.

Ehard, B, Malardel S, Dörnbrack A, Kaifler B, Kaifler N, Wedi N. Comparing ECMWF high-resolution analyses with lidar temperaturemeasurements in themiddle atmosphere. Q J R Meteorol Soc. 2018; 144:633–640. https://doi.org/10.1002/qj.3206.

European Centre for Medium-Range Weather Forecasts (2016), ECMWF IFS CY41r2 High-Resolution Operational Forecasts, https://doi.org/10.5065/D68050ZV, Research Data Archive at the National Center for Atmospheric Research, Computational and Information Systems Laboratory, Boulder, Colo. (Updated monthly) [dataset].

European Centre for Medium-Range Weather Forecasts (2019), updated monthly. ERA5 Reanalysis (0.25 Degree Latitude-Longitude Grid). Research Data Archive at the National Center for Atmospheric Research, Computational and Information Systems Laboratory. https://doi.org/10.5065/BH6N-5N20 [dataset].

Forbes, J. M., Zhang, X., Randall, C. E., France, J., Harvey, V. L., Carstens, J., & Bailey, S. M. (2021), Troposphere-mesosphere coupling by convectively forced gravity waves during Southern Hemisphere monsoon season as viewed by AIM/CIPS. Journal of Geophysical Research: Space Physics, 126, e2021JA029734. https://doi.org/10.1029/2021JA029734.

Forbes, J. M., Ern, M., & Zhang, X. (2022). The global monsoon convective system as reflected in upper atmosphere gravity waves. Journal of Geophysical Research: Space Physics, 127, e2022JA030572. https://doi.org/10.1029/2022JA030572.

Fritts, D. C., and M. J. Alexander (2003), Gravity wave dynamics and effects in the middle atmosphere, Rev. Geophys., 41(1), 1003, doi:10.1029/2001RG000106.

Gisinger, S., Polichtchouk, I., Dörnbrack, A., Reichert, R., Kaifler, B., Kaifler, N., et al. (2022). Gravity-wave-driven seasonal variability of temperature differences between ECMWF IFS and Rayleigh lidar measurements in the lee of the Southern Andes. Journal of Geophysical Research: Atmospheres, 127, e2021JD036270. https://doi.org/10.1029/2021JD036270.

Gong, J., Yue, J., and Wu, D. L. (2015), Global survey of concentric gravity waves in AIRS images and ECMWF analysis. J. Geophys. Res. Atmos., 120, 2210– 2228. doi: 10.1002/2014JD022527.

Hersbach, H, Bell, B, Berrisford, P, et al. The ERA5 global reanalysis. Q J R Meteorol Soc. 2020; 146: 1999– 2049. https://doi.org/10.1002/qj.3803.

Hoffmann, L., X. Xue, and M. J. Alexander (2013), A global view of stratospheric gravity wave hotspots located with Atmospheric Infrared Sounder observations, J. Geophys. Res. Atmos., 118, 416-434, doi:10.1029/2012JD018658.

Hoffmann, L., Wu, X., & Alexander, M. J. (2018). Satellite observations of stratospheric gravity waves associated with the intensification of tropical cyclones. Geophysical Research Letters, 45, 1692– 1700. https://doi.org/10.1002/2017GL076123.

Hoffmann, L., (2021). "AIRS/Aqua Observations of Gravity Waves", https://doi.org/10.26165/JUELICH-DATA/LQAAJA, Jülich DATA, V1. [Dataset].

Japan Meteorological Agency (JMA), http://www.jma.go.jp/jma/jma-eng/jma-center/rsmc-hp-pub-eg/besttrack.html [dataset].

Kim, S.-Y., H.-Y. Chun, and D. L. Wu (2009), A study on stratospheric gravity waves generated by Typhoon Ewiniar: Numerical simulations and satellite observations, J. Geophys. Res., 114, D22104, doi:10.1029/2009JD011971.

Kim, S. ‐ Y., and Chun, H. ‐ Y. (2011), Impact of typhoon ‐ generated gravity waves in the typhoon development, Geophys. Res. Lett., 38, L01806, doi:10.1029/2010GL045719.

Lumpe, J. D., et al. (2013), Retrieval of polar mesospheric clouds properties from CIPS: Algorithm description, error analysis and cloud detection sensitivity, *J. Atmos. Sol. Terr. Phys.,*, 104, doi:10.1016/j.jastp.2013.06.007

Liu, H., J. M. McInerney, S. Santos, P. H. Lauritzen, M. A. Taylor, and N. Pedatella (2014), Gravity waves simulated by high-resolution Whole Atmosphere Community Climate Model, Geophys. Res. Lett., 41, 9106–9112, doi:10.1002/2014GL062468.

Liu, H. ‐ L., and Vadas, S. L. (2013), Large ‐ scale ionospheric disturbances due to the dissipation of convectively ‐ generated gravity waves over Brazil, J. Geophys. Res. Space Physics, 118, 2419− 2427, doi:10.1002/jgra.50244.

Piani, C., D. Durran, M. J. Alexander, and J. R. Holton (2000), A numer- ical study of three-dimensional gravity waves triggered by deep tropical convection and their role in the dynamics of the QBO, J. Atmos. Sci., 57(22), 3689 – 3702, doi:10.1175/1520-0469(2000)057<3689:AN-SOTD>2.0.CO;2.

Preusse, P., Ern, M., Bechtold, P., Eckermann, S. D., Kalisch, S., Trinh, Q. T., and Riese, M.: Characteristics of gravity waves resolved by ECMWF, Atmos. Chem. Phys., 14, 10483–10508, https://doi.org/10.5194/acp-14-10483-2014, 2014.

Randall, C. E., et al. (2017), New AIM/CIPS global observations of gravity waves near 50–55 km, *Geophys. Res. Lett*., 44, 7044–7052, doi:10.1002/2017GL073943.

Randall, C. E., et al. (2017), AIM/CIPS Rayleigh Albedo Anomaly (RAA) dataset, https://lasp.colorado.edu/aim/ [dataset].

Rusch, D. W., G. E. Thomas, W. McClintock, A. W. Merkel, S. M. Bailey, J. M. Russell III, C. E. Randall, C. Jeppesen, and M. Callan (2009), The cloud imaging and particle size experiment on the aeronomy of ice in the mesosphere mission: Cloud morphology for the northern 2007 season, *J. Atmos. Sol. Terr. Phys.,* 71, 356–364, doi:10.1016/j.jastp.2008.11.005.

Russell, J. M., III, et al. (2009), The Aeronomy of Ice in the Mesosphere (AIM) mission: Overview and early science results, *J. Atmos. Sol. Terr. Phys.,* 71, 289-299, doi:10.1016/j.jastp.2008.08.011.

Schroeder, S., P. Preusse, M. Ern, and M. Riese (2009), Gravity waves resolved in ECMWF and measured by SABER, *Geophys. Res. Lett*., 23, 36, L10805, doi:10.1029/2008GL037054.

Vadas, S. L., Yue, J., She, C.-Y., Stamus, P. A., and Liu, A. Z. (2009), A model study of the effects of winds on concentric rings of gravity waves from a convective plume near Fort Collins on 11 May 2004, J. Geophys. Res., 114, D06103, doi:10.1029/2008JD010753.

Vadas S. L., Liu H. L. (2013), Numerical modeling of the large-scale neutral and plasma responses to the body forces created by the dissipation of gravity waves from 6 h of deep convection in Brazil, *J Geophys Res Space Phys*;118:2593–2617. doi: 10.1002/jgra.50249.

Yamashita, C., H.-L. Liu, and X. Chu (2010), Gravity wave variations during the 2009 stratospheric sudden warming as revealed by ECMWF-T799 and observations, *Geophys. Res. Lett.*, 37, L22806, doi:10.1029/2010GL045437.

Yue, J., S. L. Vadas, C.-Y. She, T. Nakamura, S. Reising, H. Liu, P. Stamus, D. Krueger, W. Lyons, and T. Li (2009), Concentric gravity waves in the mesosphere generated by deep convective plumes in the lower atmosphere near Fort Collins, Colorado, J. Geophys. Res., 114, D06104, doi:10.1029/2008JD011244.

Yue, J., L. Hoffmann, and M. Joan Alexander (2013), Simultaneous observations of convective gravity waves from a ground-based airglow imager and the AIRS satellite experiment, J. Geophys. Res. Atmos., 118, 3178–3191, doi:10.1002/jgrd.50341.

Wu, D.L. and S.D. Eckermann (2008) Global Gravity Wave Variances from Aura MLS: Characteristics and Interpretation, *J. Atmos. Sci*., 65, 3695–3718, https://doi.org/10.1175/2008JAS2489.1

Wu, J. F., Xue, X. H., Hoffmann, L., Dou, X. K., Li, H. M., and Chen, T. D. (2015), A case study of typhoon ‐ induced gravity waves and the orographic impacts related to Typhoon Mindulle (2004) over Taiwan, J. Geophys. Res. Atmos., 120, 9193− 9207, doi:10.1002/2015JD023517.

Table

Table 1. Characteristics of typhoon-generated GWs.

Name of Typhoon	Typhoon Date in 2018 (MM/DD)	Max. Wind Speed (Duration >100kt)	GW Analysis Date	λ_h (km)	λ_z (km)	w' (GW) Amplitude at 20 km	w' (GW) Amplitude at 40 km
Yutu	10/21 – 11/03	115 kt (78 h)	10/27	~ 250	~10-14	2.2 cm/s	6.4 cm/s
Jebi	08/26 – 09/04	105 kt (48 h)	09/02	~150	~15	2.6 cm/s	8.1 cm/s
Mangkhut	09/06 – 09/17	110 kt (90 h)	09/14	~150-400	~10-17	2.8 cm/s	6.3 cm/s
Kong-rey	09/28 – 10/06	115 kt (48 h)	10/02	~200	~10	2.3 cm/s	4.4 cm/s
Trami	09/20 – 10/01	105 kt (48 h)	09/28	~270	~10-12	2.5 cm/s	4.8 cm/s

Figures

Figure 1. (a) Path of Typhoon Yutu from October 22 to November 1. (b) Maximum sustained wind speed (10-minute average) along the path of Typhoon Yutu.

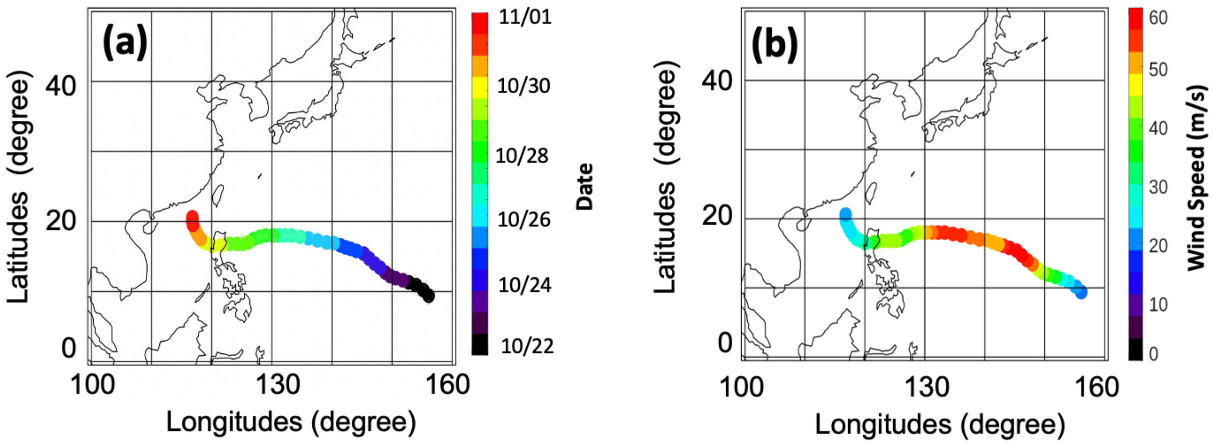

Figure 2. Snapshots of concentric GW observations from (a) CIPS RAA (%) at ~50-55 km and (b) AIRS brightness temperature perturbation (K) at ~30-40 km and vertical wind perturbation from (c, d) ECMWF and (e, f) ERA5 at 1 hPa (~50 km) and 10 hPa (~30 km). AIRS and CIPS observations were made on October 27, ~4:30 UT and October 26, ~22:25 UT, respectively. ERA5 and ECMWF plots are made with data from October 27, 00 UT. Red boxes indicate +/- 15 degree from the center of typhoon location.

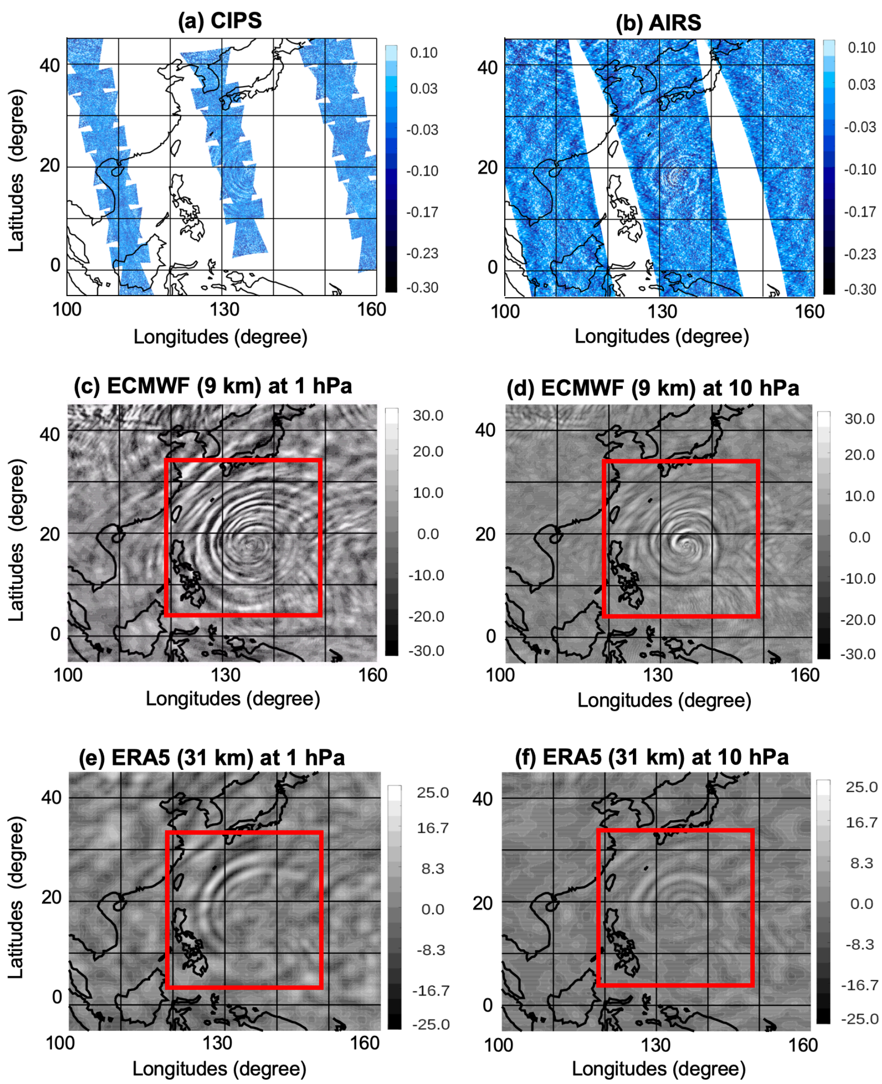

Figure 3. Vertical wind perturbation (cm/s) from ECMWF-IFS at 40, 10, 3.7, 1.31, 0.86, and 0.25 hPa for Typhoon Yutu on October 27 at 00 UT.

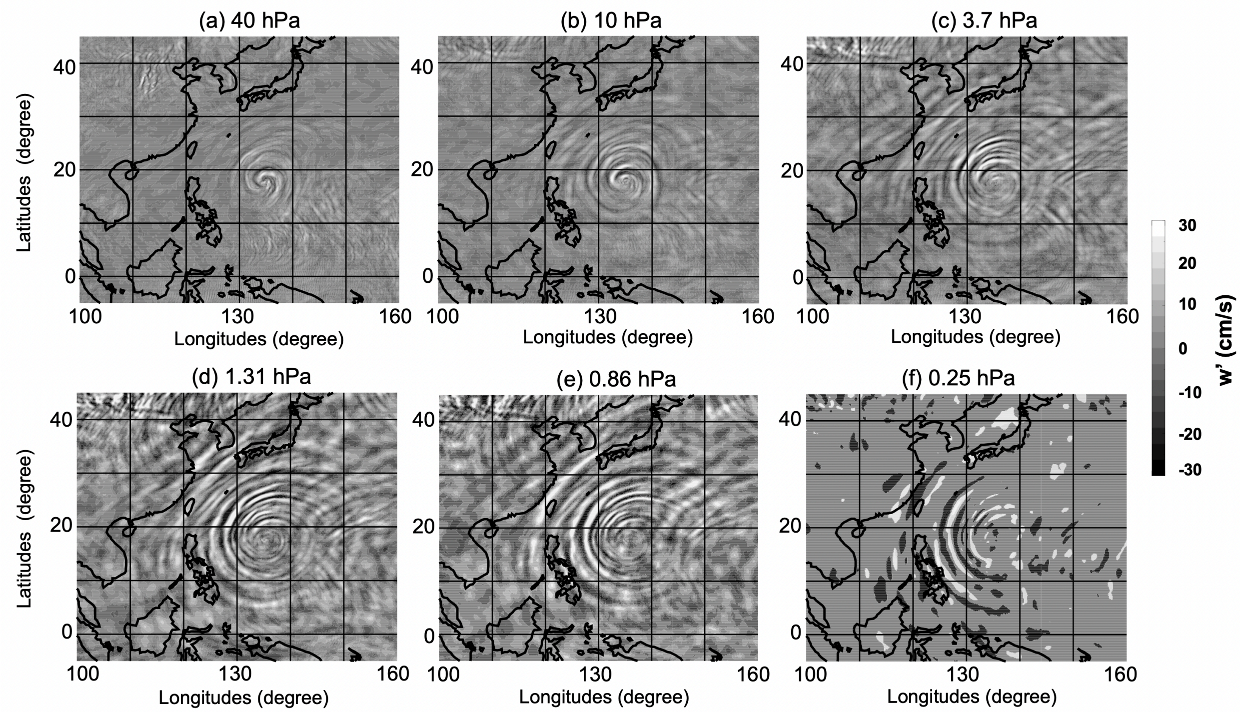

Figure 4. Power spectrum of horizontal wavelength for (a, b) AIRS brightness temperature perturbations (K), (c, d) CIPS RAA (%), and (e, f) ECMWF vertical wind perturbation (cm/s) at 1 hPa (~50 km). Red thick lines indicate data used to calculate the power spectrum.

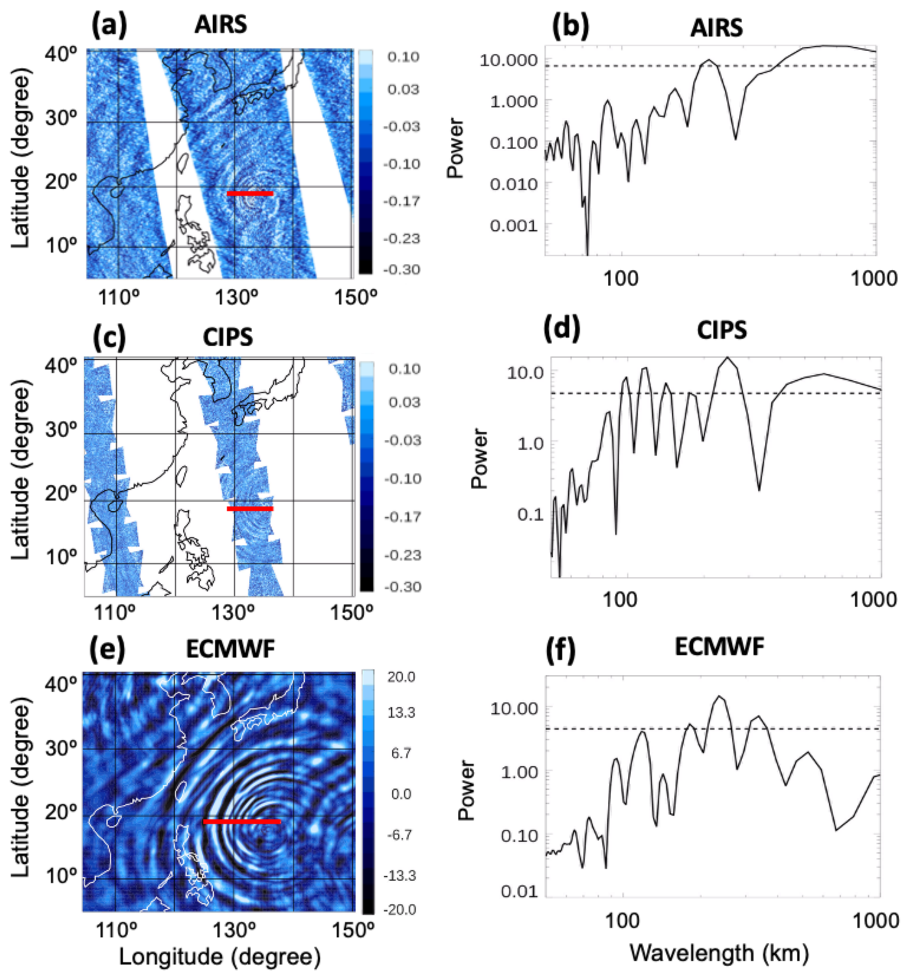

Figure 5. Snapshots of vertical wind GW perturbation from October 23 to October 31 at 3 hPa (~40 km) (top) and at 300 hPa (~10 km) (bottom). White lines indicate continents.

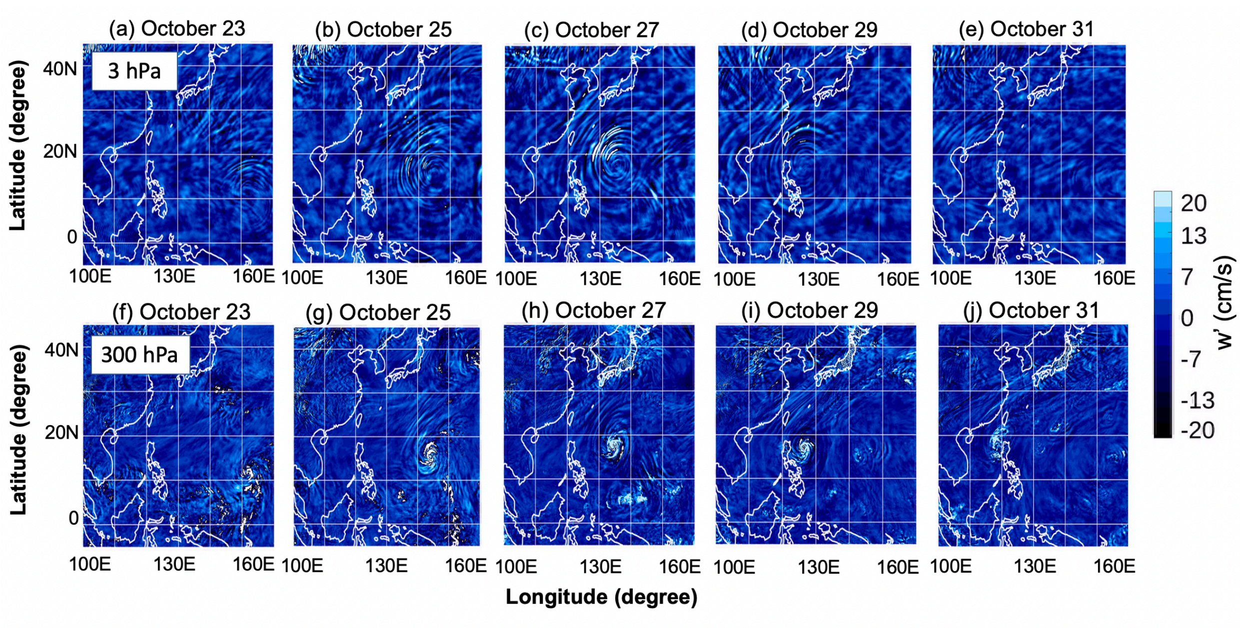

Figure 6. (a) Snapshot of concentric vertical wind GW perturbation at 5 hPa (~35 km) on October 27, 2018 at 00 UT and (b) vertical slice at white transect in Figure 6a.

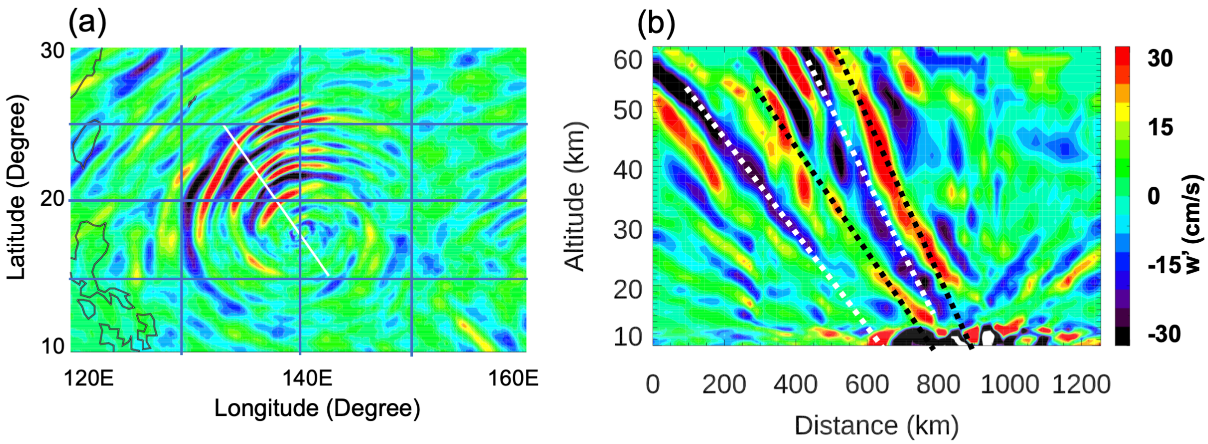

Figure 7. Averaged GW vertical wind (w) amplitudes at (black) 3 hPa (~40 km) and (red) 10 hPa (~30 km) from (a) 6-hourly ECMWF data and (b) hourly ERA5 data, and Typhoon Yutu maximum sustained wind speed provided by Japanese Meteorological Agency (JMA) from October 22 to November 1, 2018.

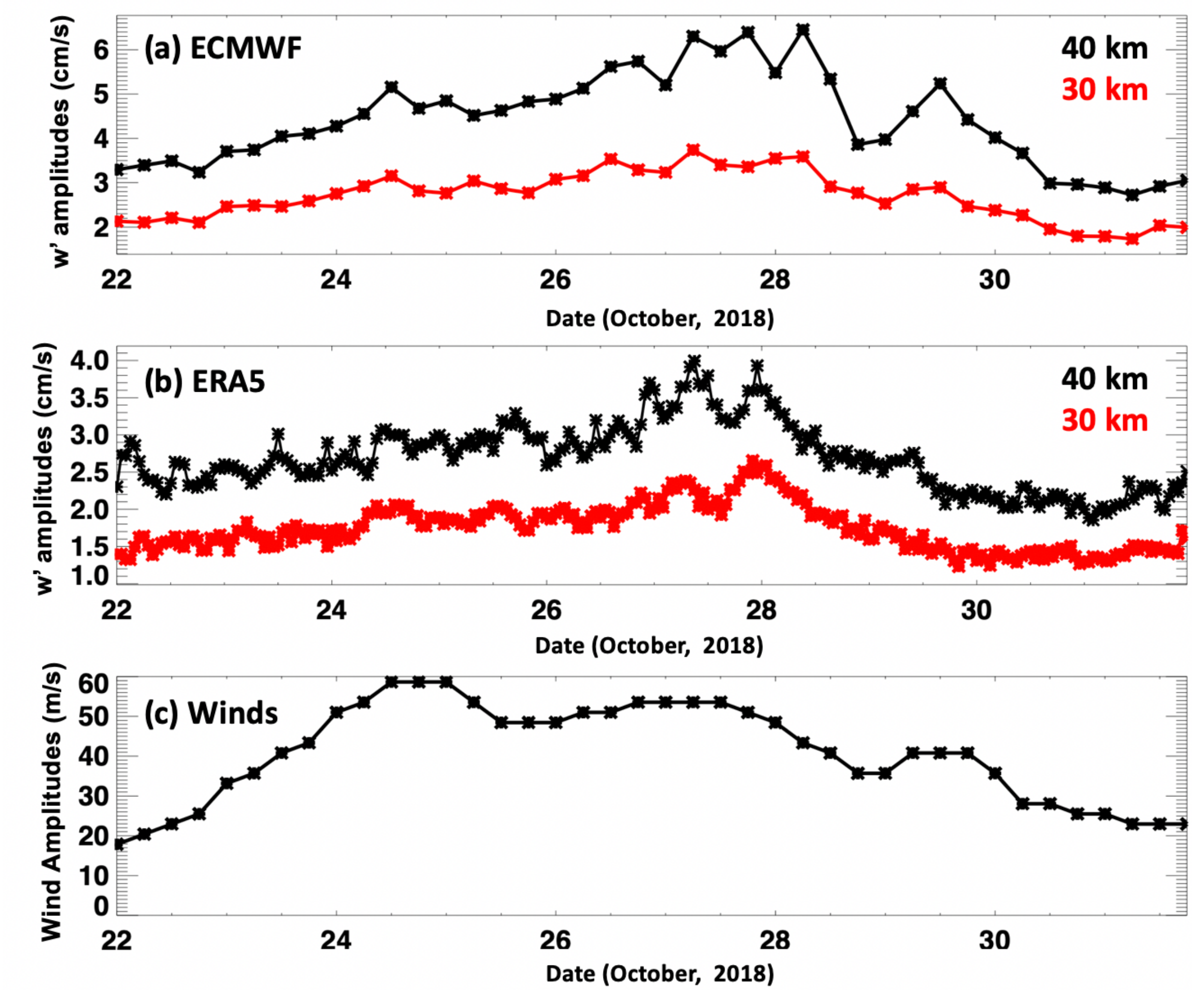

Figure 8. Gravity wave momentum fluxes (x10^{-4} Pa; color contours) on October 27, 2018 at 00 UT at (a) 2 hPa, (b) 5 hPa, (c) 10 hpa, and (d) 50 hPa. Arrows indicate horizontal wind directions and magnitudes.

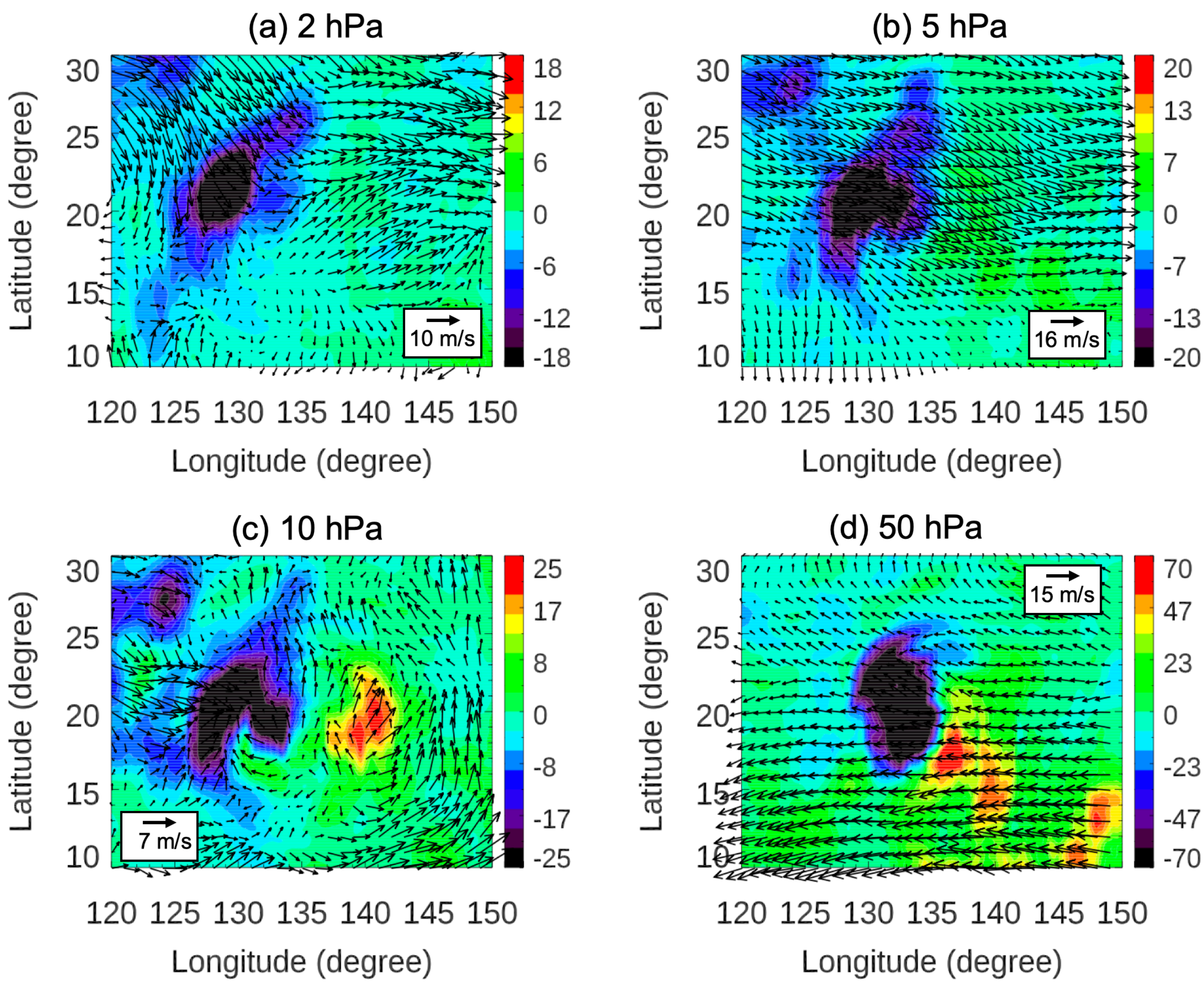

Figure 9. (a-d) Concentric gravity wave structures in the ECMWF vertical wind at 5 hPa (~35 km) altitude; (e-h) vertical slices of vertical wind GW perturbation at the white transects in (a-d), respectively; and (i-l) corresponding power spectrum density at ~35 km for four each typhoon case.

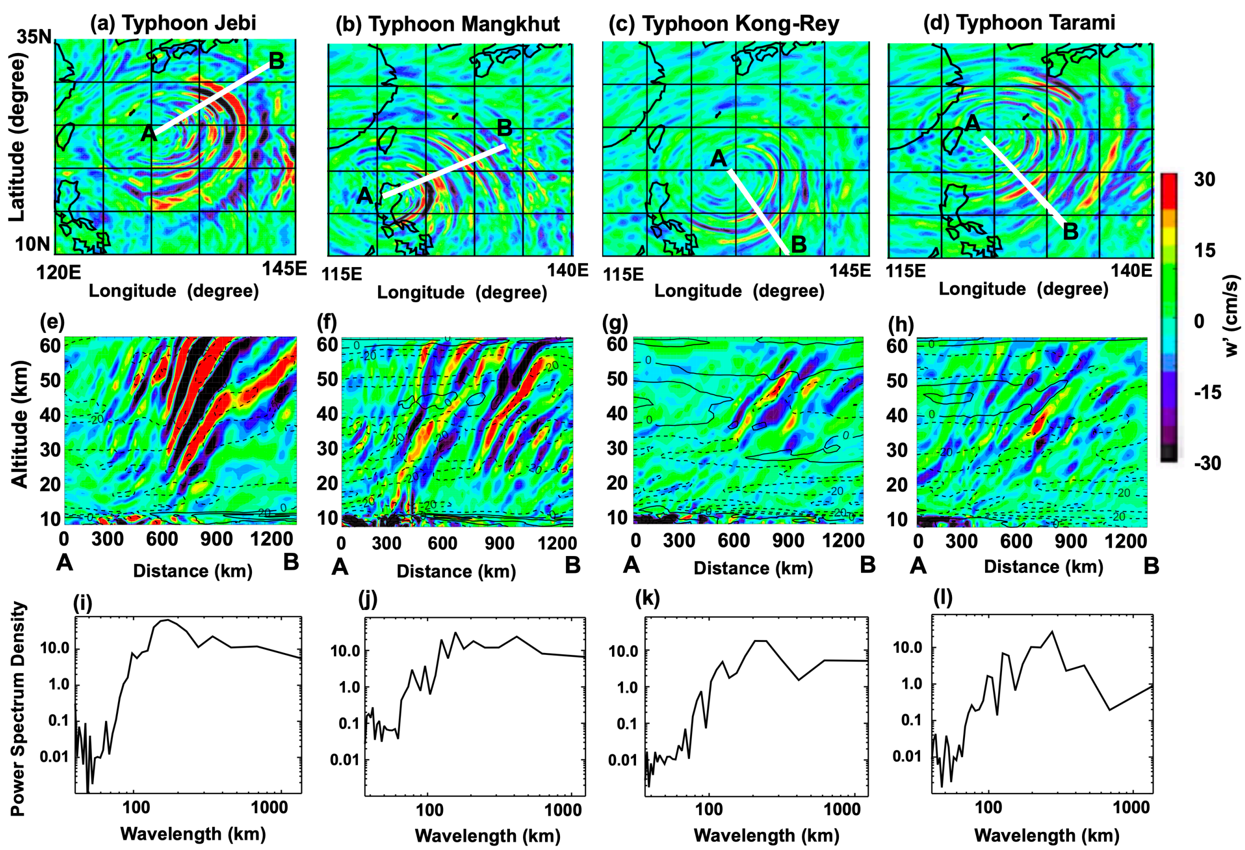

Figure 10. (contours) Vertical wind perturbation and (black arrows) horizontal wind vectors at ~35 km for (a) Typhoon Yutu on October 27, (b) Typhoon Jebi on September 2, (c) Typhoon Mangkhut on September 14, (d) Typhoon Kong-Rey on October 2, and (e)Typhoon Trami on September 28. Red thick arrows indicate wave propagation directions.